A Fast All-sky Radiation Model for Solar applications with Narrowband Irradiances on Tilted surfaces (FARMS-NIT): Part I. The clear-sky model

Yu Xie*, Manajit Sengupta

Power Systems Engineering Center, National Renewable Energy Laboratory, Golden, CO 80401, United States

ARTICLE INFO

ABSTRACT

The solar energy industry often uses individual steps to empirically compute plane-of-array (POA) irradiance from horizontal irradiance and decompose it to narrow-wavelength bands. Conventional radiative transfer models designed for meteorological applications requires significant computing efforts in practice; however, they provide a physics-based solution of radiance and therefore are capable of computing spectral POA irradiances in a single step. In this study, we integrate the advantages of the current models and develop an innovative radiative transfer model, the Fast All-sky Radiation Model for Solar applications with Narrowband Irradiances on Tilted surfaces (FARMS-NIT), to efficiently compute irradiances on inclined photovoltaics (PV) panels for 2002 narrow-wavelength bands from 0.28 to 4.0 μm. This study is reported in two parts. Part I presents the methodology and performance evaluation of the new model under clear-sky conditions. The Simple Model of the Atmospheric Radiative Transfer of Sunshine (SMARTS), which was designed to compute clear-sky irradiances, is employed to rapidly provide the optical properties of a given clear-sky atmosphere. The clear-sky radiances in the narrow-wavelength bands are computed by considering three paths of photon transmission and solving the radiative transfer equation with the single-scattering approximation. The Bi-directional Transmittance Distribution Function (BTDF) of aerosols is given by their single-scattering phase function with a correction using a two-stream approximation. The validation analysis confirms that FARMS-NIT has improved accuracy compared to TMYSPEC as evaluated by both surface observations and a state-of-the-art radiative transfer model. This model substantially improves computational efficiency compared to other radiative transfer models though it uses slightly more computing time than TMYSPEC. Part II of this study addresses the model in cloud-sky conditions and will be published as a companion paper.

1. Introduction

The increasing use of solar energy as an alternative to conventional energy sources has boosted the demand to precisely measure or simulate solar resource at the land surface. Solar radiation data are routinely provided on horizontal surfaces by ground- (Stokes and Schwartz, 1994) and satellite-based observations (Sengupta et al., 2014, 2018; Xie et al., 2016) in a broadband wavelength range 0.2–5 μm because ≈99% of the total solar radiation on the Earth's surface lies in this region (Liou, 2002).

Quantification of solar radiation in narrow-wavelength bands plays a crucial role in solar energy research because the efficiency of photovoltaic (PV) systems is dominated by the spectral distribution of incident solar radiation, the spectral response of semiconductor materials,

and the solar cell designs to split spectral radiation (Fahrenbruch and Bube, 1983; Mojiri et al., 2013). Although high-spectral-resolution models designed for meteorological applications—e.g., the line-by-line model (Clough et al., 2005)—are capable of computing spectral solar radiation based on fundamental physics, they are often time-consuming when solving the absorption coefficients of the molecular species in the atmosphere. Thus, models parameterizing the computation of absorption and scattering—e.g., the Simple Model of the Atmospheric Radiative Transfer of Sunshine (SMARTS) (Gueymard, 1995), SUNSPEC (McCluney and Gueymar, 1993), and TMYSPEC (Myers, 2012)—were developed to provide efficient solutions of spectral radiation and thus are more applicable to solar energy applications.

At the land surface, three solar sources contribute to plane-of-array (POA) irradiances in broad or narrow wavelength bands: direct radiation, diffuse radiation from sky, and diffuse radiation from the land
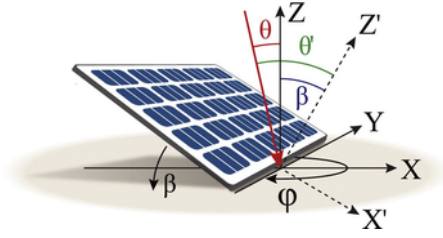

Fig. 1. Geometry a PV panel. XYZ represents a three-dimensional Cartesian coordinate on the horizontal surface. X'YZ' represents a three-dimensional Cartesian coordinate on the PV panel. The red beam represents a solar beam.
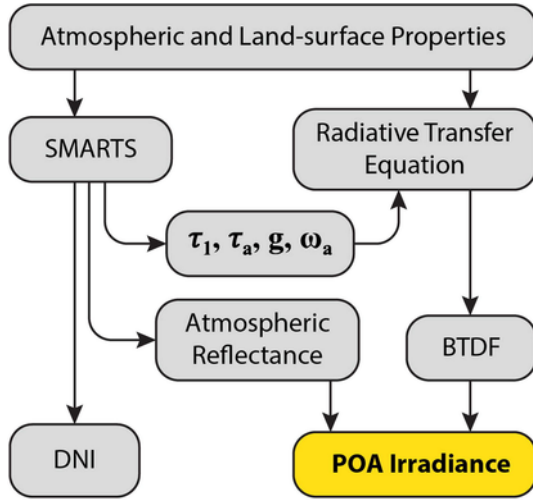

Fig. 2. A flowchart of the FARMS-NIT model for a clear-sky condition.

surface (Xie et al., 2018). Transposition models, which convert horizontal irradiance to the POA, simulate the contribution from diffuse radiation by following empirical regression analyses (hereafter referred to as empirical models) based on long-term observations of diffuse horizontal irradiance (DHI) and POA irradiances in various orientations (Perez et al., 1990; Reindl et al., 1990) or by assuming that diffuse radiation is isotropic over the sky dome (hereafter referred to as isotropic models) (Badescu, 2002; Liu and Jordan, 1961). Compared to empirical models, isotropic models underestimate the strong forward scattering by clouds or aerosols (Xie, 2010; Xie et al., 2011, 2009, 2012), and thus they are likely to underestimate POA irradiance on 1- or 2-axis tracking PV panels; however, the performance of empirical models depends on the localized atmospheric and land surface conditions as well as solar and PV orientations (Xie et al., 2018). Xie et al. (2018) demonstrated that POA irradiance can be calculated using the spatial distribution of radiances that are computed by one-dimensional radiative transfer models designed for meteorological purposes.

Xie et al. (2016) developed the Fast All-sky Radiation Model for Solar applications (FARMS), which uses the parameterization of clear-sky radiation and physics-based solutions of cloud transmittance and reflectance to efficiently compute broadband global horizontal irradiance (GHI) and direct normal irradiance (DNI). This study intends to expand the capability of FARMS and develop a new radiative transfer model, FARMS with Narrowband Irradiances on Tilted surfaces (FARMS-NIT), which integrates the advantages in the existing models used for meteorological and solar energy purposes. This new model is based on efficient computation of spectral radiances at the land surface, which simultaneously leads to POA irradiances in numerous narrow-wavelength bands.

This study is reported in two parts: Part I (this paper) introduces the algorithm and performance evaluation of FARMS-NIT under clear-sky conditions where the aerosol absorption and scattering is represented by the single-scattering approximation with the correction using a two-stream method (Meador and Weaver, 1980; Xie and Liu, 2013; Xie et al., 2014); Part II (to be published as a companion paper) computes solar radiances and POA irradiances under cloudy-sky conditions where the cloud transmittances and reflectances are precomputed for narrow-wavelength bands from 0.28 to 4.0 μm.

2. Methodology

2.1. Computation of spectral POA irradiance

A spectral POA irradiance over a monofacial PV panel can be given by

$$POAI = POAI_d + POAI_{u,sky} + POAI_{u,ground}, \tag{1}$$

where $POAI_d$, $POAI_{u,sky}$, and $POAI_{u,ground}$ are the spectral POA irradiances associated with direct irradiance, diffuse irradiance from sky, and diffuse irradiance from ground reflection, respectively (Gueymard, 1987; Jakhrani et al., 2012; Loutzenhiser et al., 2007; Noorian et al., 2008; Xie et al., 2018).

According to Xie et al. (2018) and the references citied therein, $POAI_d$, $POAI_{u,sky}$, and $POAI_{u,ground}$ can be computed by

$$POAI_d = DNI\cos\theta' \tag{2a}$$

$$POAI_{u,sky} = \int_0^{2\pi} \int_0^{\Theta(\beta,\varphi)} I_t \cos\theta' \sin\theta d\theta d\varphi \tag{2b}$$

$$POAI_{u,ground} = \int_0^{2\pi} \int_0^{\frac{\pi}{2}-\Theta(\beta,\varphi)} I_r \cos\theta' \sin\theta d\theta d\varphi, \tag{2c}$$

where *DNI* denotes direct normal irradiance; I_t is the diffuse radiance from the sky; I_r is the reflected radiance by the land surface; θ' is the angle between incident solar beam and the normal direction of the in-
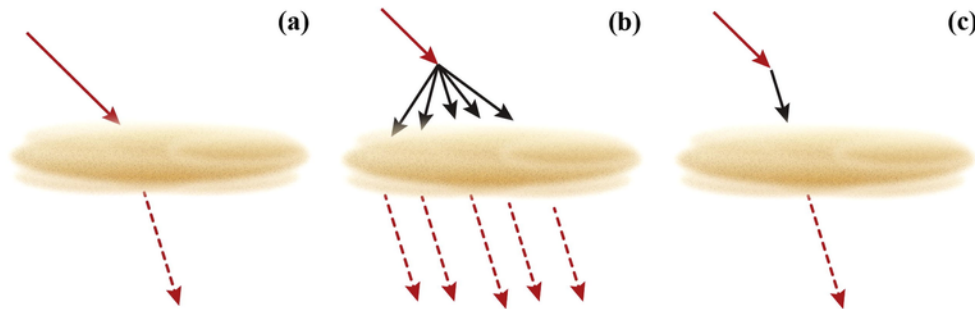

Fig. 3. Partitioning transmittance of the atmosphere where solar radiation is (a) absorbed by the atmosphere and scattered by aerosol; (b) scattered in the atmosphere and scattered again by aerosol; and (c) scattered in the atmosphere and absorbed by aerosol.
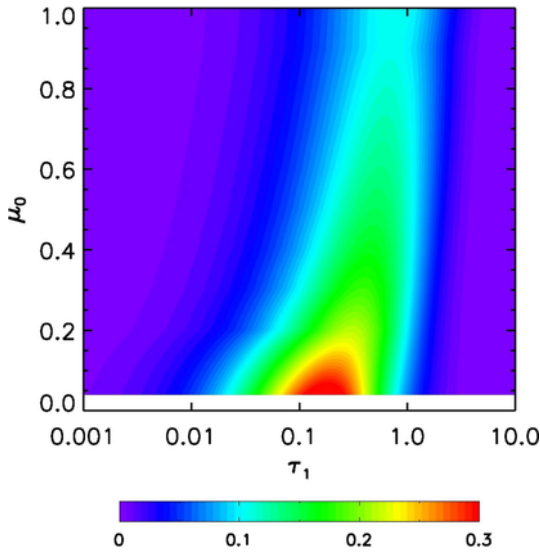
Fig. 4. TF_{0u}/ω_1 computed as a function of μ_0 and τ_1 using Eq. (19). TF_{0u} is the diffuse transmittance of the clear atmosphere where the incident is direct radiation; ω_1 is the single-scattering albedo of Rayleigh scattering; τ_1 is the optical thickness of the clean atmosphere. μ_0 is the cosine value of the solar zenith angle.
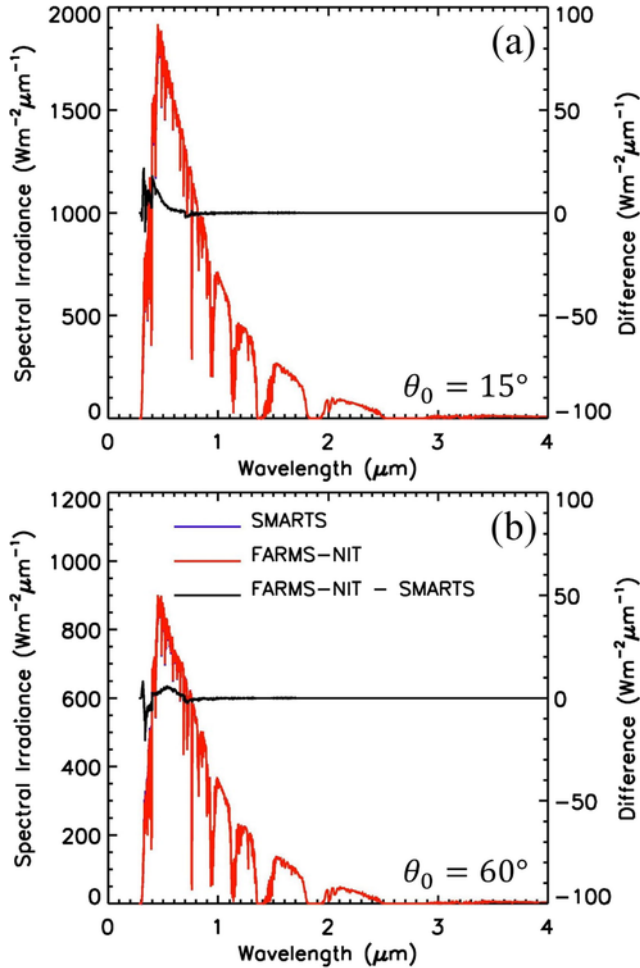

Fig. 5. Spectral irradiances for a clean atmosphere over a horizontal surface computed by SMARTS and FARMS-NIT when (a)$\theta_0 = 15°$ and (b) $\theta_0 = 60°$. The red and blue lines represent the simulations by FARMS-NIT and SMARTS, respectively, and the black line denotes their difference. (For interpretation of the references to colour in this figure legend, the reader is referred to the web version of this article.)

clined PV panel; θ is zenith angle; φ is azimuth angle; β is the title angle of the PV panel; and $\Theta(\beta, \varphi)$ represents the upper limit of θ for each φ that can be given by

$$\Theta(\beta, \varphi)$$
$$= \begin{cases} \frac{\pi}{2} & when -\frac{\pi}{2} \le \varphi \le \frac{\pi}{2} \\ \frac{\pi}{2} - \tan^{-1}(-\tan\beta\cos\varphi) & when \frac{\pi}{2} \le \varphi \le \frac{3\pi}{2} \end{cases} \quad . \tag{2d}$$

The geometry of a PV panel and variables used in Eq. (2) are illustrated in Fig. 1. Thus, POA irradiance can be computed by Eq. (2) without any approximation when I_t and I_r are known.

2.2. Computation of spectral radiances in the atmosphere

Fig. 2 denotes a flowchart showing the computation of clear-sky POA irradiance by FARMS-NIT. To compute I_t and I_r, we assume a homogeneous aerosol layer in the atmosphere around the land surface. Therefore, the atmosphere can be divided into two layers: the aerosol layer and the atmosphere above it. For DNI, we follow the solutions from SMARTS, version 2.9.5, (Gueymard, 1995) which parameterizes the spectral transmission of direct solar radiation under clear-sky conditions. With users' input of atmospheric profile and aerosol information, SMARTS can also compute the reflectance of the atmosphere, the total optical thickness of all trace gases, τ_1, aerosol optical depth (AOD), τ_a, and the single-scattering albedo, ω_a, and asymmetric factor, g, of the aerosol. The computed optical thickness of trace gases and aerosol properties in spectral bands are then input to the radiative transfer equation and used to solve the Bi-directional Transmittance Distribution Function (BTDF) of the clear atmosphere. Therefore, the spectral region and resolution of FARMS-NIT follow SMARTS, which covers 2002 narrow-wavelength bands within 0.28–4.0 μm, and uses intervals of 0.5 nm, 1 nm, and 5 nm intervals in 0.28–0.3995 μm, 0.4–1.7 μm and 1.705–4.0 μm, respectively (Gueymard, 1995).

The diffuse radiances at the land surface are computed by

$$I_t(\mu_t, \varphi_t) = I_0(TF_1 + TF_2) \tag{3a}$$

$$I_0 = \frac{\mu_0 F_0}{\pi}, \tag{3b}$$

where TF_1 is the BTDF for the first-order radiation; TF_2 is the BTDF for radiances related to multiple reflection between aerosols and the land surface; μ_0 is the cosine value of the solar zenith angle; and I_0 and F_0 are the extraterrestrial solar radiance and irradiance, respectively.

The optical thickness of Rayleigh scattering is very small, especially in the near-infrared and infrared regions ($\lambda > 0.7$ μm). Thus, the scattering events in the clean atmosphere—i.e. cloud and aerosol free—are assumed as single scattering. The effect of multiple scattering in the Ultraviolet (UV) and visible regions is considered and discussed in the next section.

Wang et al. (2013) derived the Bi-directional Reflectance Distribution Function (BRDF) of the atmosphere from six possible paths of photon transmission. Following the Rayleigh scattering correction technique and the study of Wang et al. (2013), TF_1 can be solved from three independent events (see Fig. 3) where photons are (a) absorbed by the atmosphere and scattered by aerosol, (b) scattered in the atmosphere and scattered again by aerosol, and (c) scattered in the atmosphere and absorbed by aerosol. Thus, TF_1 is given by

$$TF_1 = TF_{1a} + TF_{1b} + TF_{1c} \tag{4}$$

$$TF_{1a} = exp\left(-\frac{\tau_1}{\mu_0}\right) TF_{0t}^a \tag{5a}$$
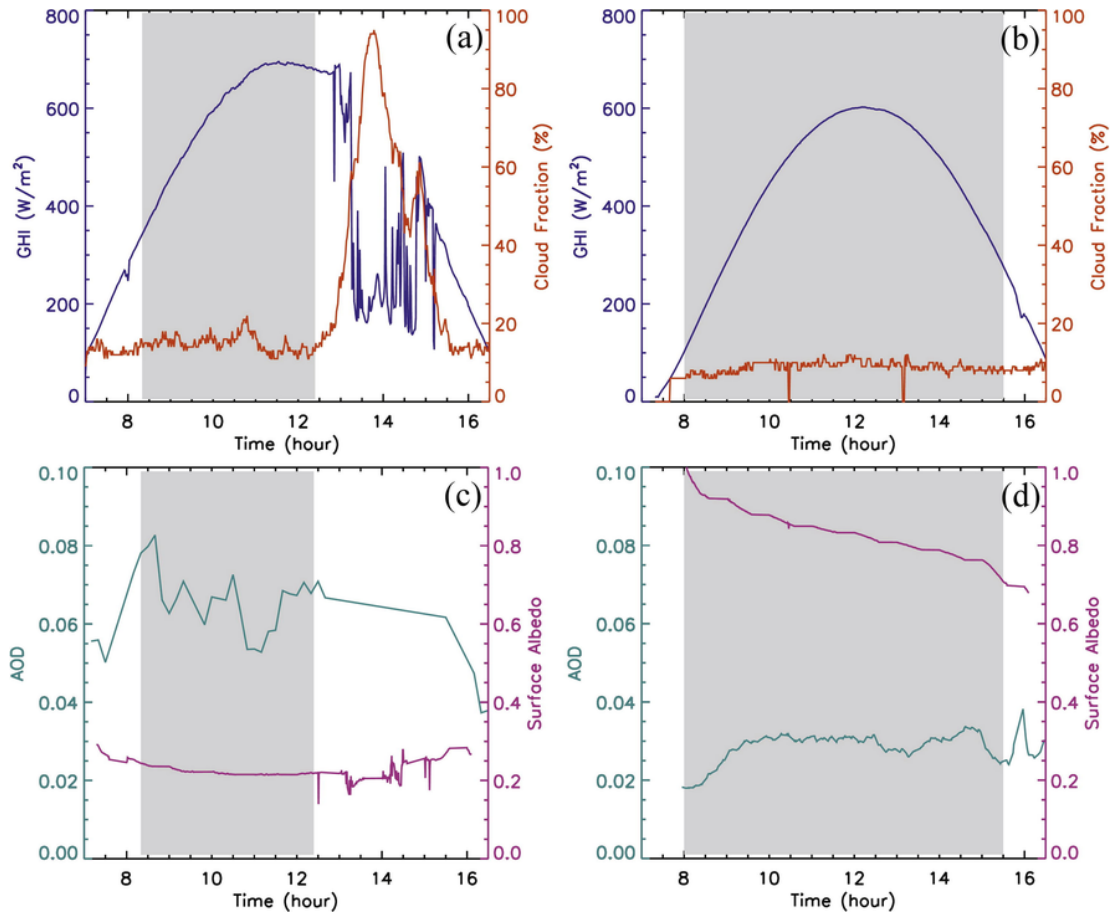
3

Fig. 6. Observations of GHI and cloud fraction at NREL on (a) October 20, 2017 and (b) January 22, 2018. Observations of AOD and surface albedo at NREL on (c) October 20, 2017 and (d) January 22, 2018.

$$\text{TF}_{1b} = \frac{\omega_1}{4\pi} \int_0^{2\pi} \int_0^1 \frac{\mu_j}{\mu_j - \mu_0} P_{0j} \text{TF}_{jt}^a \left[\exp\left(-\frac{\tau_1}{\mu_j}\right) - \exp\left(-\frac{\tau_1}{\mu_0}\right) \right] d\mu_j d\varphi_j \tag{5b}$$

$$\text{TF}_{1c} = \frac{\omega_1 P_{0t}}{4(\mu_t - \mu_0)} \exp\left(-\frac{\tau_a}{\mu_t}\right) \left[\exp\left(-\frac{\tau_1}{\mu_t}\right) - \exp\left(-\frac{\tau_1}{\mu_0}\right) \right], \tag{5c}$$

where TF_{1a}, TF_{1b}, and TF_{1c} represent TF_1 for the independent events; TF_{0t}^a and TF_{jt}^a are BTDFs of the aerosol; P_{0j} and P_{0t} are the single-scattering phase functions of Rayleigh scattering; ω_1 is the single-scattering albedo of Rayleigh scattering in the atmosphere; μ is the cosine value of zenith angle; and the subscripts, "j", "0", and "t" represent the photon direction after the scattering and the solar incident and outgoing directions, respectively. Details on the derivation of Eq. (5) are given in Appendix A.

With the assumption that energy is conserved in the Rayleigh scattering process, ω_1 can be approximated by Wang et al. (2013):

$$\omega_1 = \frac{\tau_R}{\tau_1}, \tag{6}$$

where τ_R is the optical thickness associated with Rayleigh scattering. P_{0j} and P_{0t} are given by the phase function of Rayleigh scattering (Liou, 2002):

$$P_{0j} = \frac{3}{4}\left(1 + \cos^2\Theta_{0j}\right) \tag{7a}$$

and

$$P_{0t} = \frac{3}{4}\left(1 + \cos^2\Theta_{0t}\right), \tag{7b}$$

where Θ_{0j} and Θ_{0t} are the scattering angles according to the photon incident and outgoing directions. For backward scattering, Θ_{0j} and Θ_{0t} are given by

$$\cos\Theta_{0j} = -\mu_0\mu_j + \left(1 - \mu_0^2\right)^{1/2}\left(1 - \mu_j^2\right)^{1/2}\cos\varphi_{0j} \tag{8a}$$

and

$$\cos\Theta_{0t} = -\mu_0\mu_t + \left(1 - \mu_0^2\right)^{1/2}\left(1 - \mu_t^2\right)^{1/2}\cos\varphi_{0t}, \tag{8b}$$

where φ_{0j} and φ_{0t} denote relative azimuth angle between the photon incident and outgoing directions. For forward scattering, Θ_{0j} and Θ_{0t} are given by

$$\cos\Theta_{0j} = \mu_0\mu_j + \left(1 - \mu_0^2\right)^{1/2}\left(1 - \mu_j^2\right)^{1/2}\cos\varphi_{0j} \tag{8c}$$

and

$$\cos\Theta_{0t} = \mu_0\mu_t + \left(1 - \mu_0^2\right)^{1/2}\left(1 - \mu_t^2\right)^{1/2}\cos\varphi_{0t}, \tag{8d}$$

Because aerosols in the atmosphere are optically very thin, we assume single scattering within the aerosol layer as the first-order ap-
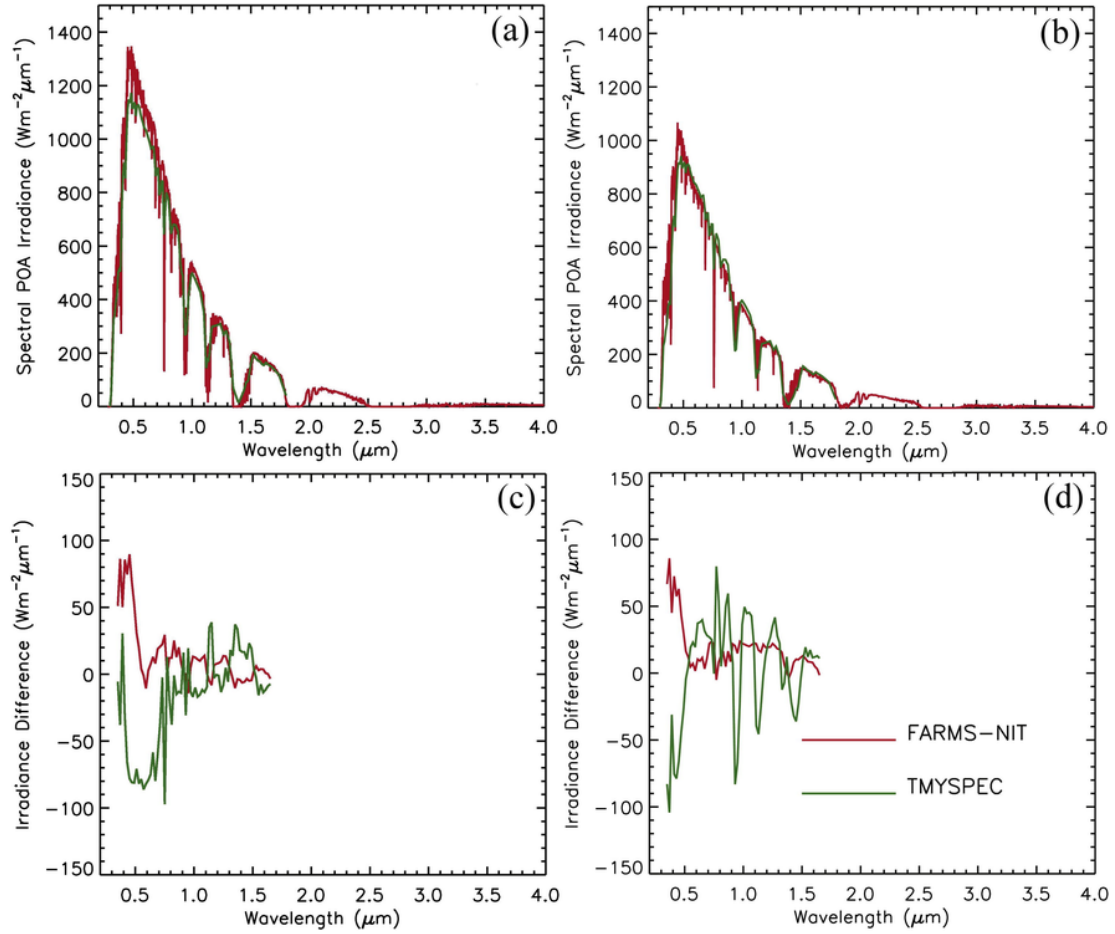
Fig. 7. Comparison of spectral POA irradiances computed by FARMS-NIT and TMYSPEC (a) at 10:05 am on October 20, 2017, and (b) 12:00 pm on January 22, 2018. Difference between model simulation and NREL observations on a single-axis tracker (c) at 10:05 am on October 20, 2017 and (d) 12:00 pm on January 22, 2018.

Table 1
MBE, MAE, PE, APE, MPE, and MAPE of computed spectral irradiances in the POA using FARMS-NIT and TMYSPEC.

	MBE ($Wm^{-2}\mu m^{-1}$)	MAE ($Wm^{-2}\mu m^{-1}$)	PE (%)	APE (%)	MPE (%)	MAPE (%)
October 20, 2017						
FARMS-NIT	9.64	15.31	1.86	2.96	−2.03	6.78
TMYSPEC	−17.96	30.29	−3.47	5.85	20.32	27.4
January 22, 2018						
FARMS-NIT	11.13	17.92	2.28	3.67	1.94	5.57
TMYSPEC	−79.47	90.96	−16.27	18.62	−17.66	22.47

proximation. Under this assumption, TF_{0t}^a and TF_{jt}^a can be given as

$$TF_{0t}^a = \frac{\omega_a}{4} P_{0t}^a \frac{1}{\mu_0 - \mu_t} \left[exp\left(-\frac{\tau_a}{\mu_0}\right) - exp\left(-\frac{\tau_a}{\mu_t}\right) \right] \tag{9a}$$

$$TF_{jt}^a = \frac{\omega_a}{4} P_{jt}^a \frac{1}{\mu_j - \mu_t} \left[exp\left(-\frac{\tau_a}{\mu_j}\right) - exp\left(-\frac{\tau_a}{\mu_t}\right) \right], \tag{9b}$$

where P_{0j}^a and P_{jt}^a are the single-scattering phase functions of aerosol that can be approximated by the asymmetric factor of aerosol, g, and Henyey-Greenstein phase function:

$$P_{0t}^a = \frac{1 - g^2}{\left(1 + g^2 - 2g\cos\Theta_{0t}\right)^{3/2}} \tag{9c}$$

$$P_{jt}^a = \frac{1 - g^2}{\left(1 + g^2 - 2g\cos\Theta_{jt}\right)^{3/2}}. \tag{9d}$$

The asymmetric factors of aerosol are following the results from SMARTS for all the narrow bands. Details on the derivation of TF_{0t}^a and TF_{jt}^a can be found in Appendix B. The impact of multiple scattering on Eqs. ((6) and (9)) will be discussed in the next section.

For computing TF_2, the first-order downwelling irradiance is derived as

$$F_1 = F_d + \int_0^{2\pi} \int_0^1 I_0 TF_1 \mu_t d\mu_t d\varphi_t, \tag{10}$$
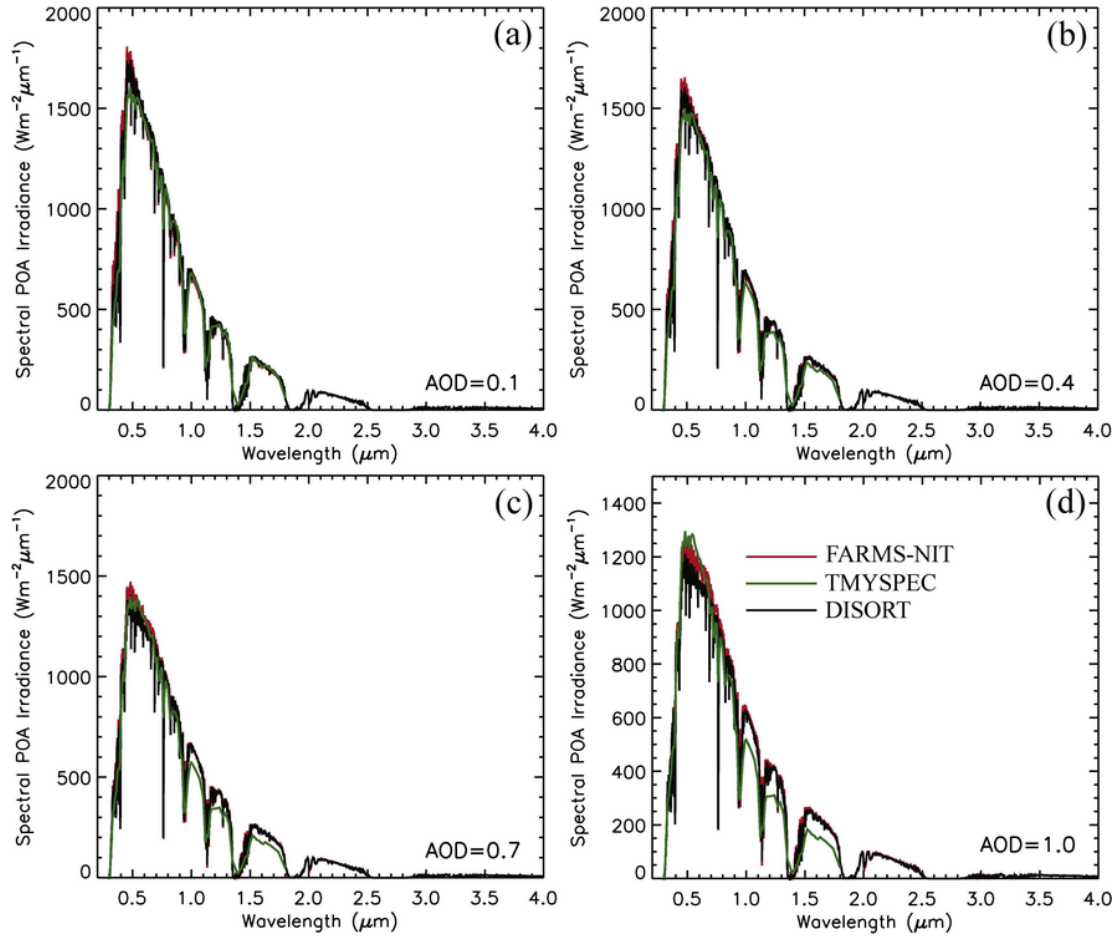
Fig. 8. Comparison of spectral POA irradiances computed by FARMS-NIT, TMYSPEC, and DISORT at 12:00 pm on October 20, 2017, when the solar zenith angle is 50.447°. A PV panel is assumed facing south with a tilt angle of 30°.

where F_d represents direct radiation on the horizontal surface. The total downwelling irradiance is then

$$
\begin{aligned}
F_{\text{total}} &= F_1 + F_1 R_s R_{\text{uu}} + F_1 R_s R_{\text{uu}} R_s R_{\text{uu}} + \cdots \\
&= F_1 \left(1 - R_s R_{\text{uu}} \right)^{-1},
\end{aligned}
\tag{11}
$$

where R_s is the land-surface albedo, and R_{uu} is the clear-sky reflectance of irradiance that is computed by SMARTS. Then TF_2 can be derived as follows:

$$
\mu_0 F_0 TF_2 = F_{\text{total}} - F_1 = \frac{R_s R_{\text{uu}}}{1 - R_s R_{\text{uu}}} F_1
\tag{12a}
$$

$$
TF_2 = \frac{R_s R_{\text{uu}}}{1 - R_s R_{\text{uu}}} \frac{F_1}{\mu_0 F_0}.
\tag{12b}
$$

With the assumption of a Lambertian surface, the reflected radiance by the land surface can be computed by

$$
I_r = \frac{F_{total} R_s}{\pi}.
\tag{13}
$$

2.3. Impact of multiple-scattering in the atmosphere

In this derivation of TF_1, we assume that the Rayleigh scattering in the atmosphere and the light scattering within the aerosol are single-scattering events; however, the optical thickness related to Rayleigh scattering might not be very small in certain UV and visible regions. To account for the effect of multiple scattering due to Rayleigh scattering, the single-scattering albedo of the clean atmosphere in Eq. (6) is adjusted to

$$
\omega_1 = \frac{\tau_R}{\tau_1} M,
\tag{14a}
$$

where M is a scaling factor for multiple scattering that is given by

$$
M = \begin{cases} 1 & when\ 0.28\ \mu m \leq \lambda \leq 0.3\ \mu m\ or\ 0.7\ \mu m \leq \lambda \leq 4.0\ \mu m \\ 1.6232711\tau_R + 1.0439955 & when\ 0.3\ \mu m < \lambda < 0.7\ \mu m \end{cases}.
\tag{14b}
$$

Determination of the scaling factor for multiple scattering can be found in Appendix C.

Moreover, the amount of aerosol over desert or high-polluted areas can be significant, which also leads to multiple scattering of solar radiation within the aerosol. To account for this effect, we consider the two-stream approximation provided by Meador and Weaver (1980) where a thin layer transmittance of irradiance is given by

$$
T_{0u}^a = 1 - \frac{\tau_a}{\mu_0} \left[1 + \omega_a \left(0.5 - 0.5g \right) - \omega_a \right] - exp \left(-\frac{\tau_a}{\mu_0} \right).
\tag{15}
$$

To make the GHI consist with the two-stream approximation, Eqs. ((9a) and (9b)) are adjusted by

Fig. 10. Computing time of hourly spectral POA irradiances during a day.

Fig. C. Scaling factors of multiple scattering as functions of τ_R when $0.3\,\mu m < \lambda < 0.7\,\mu m$. The black line denotes the fitting curve of the scaling factors for USSA.
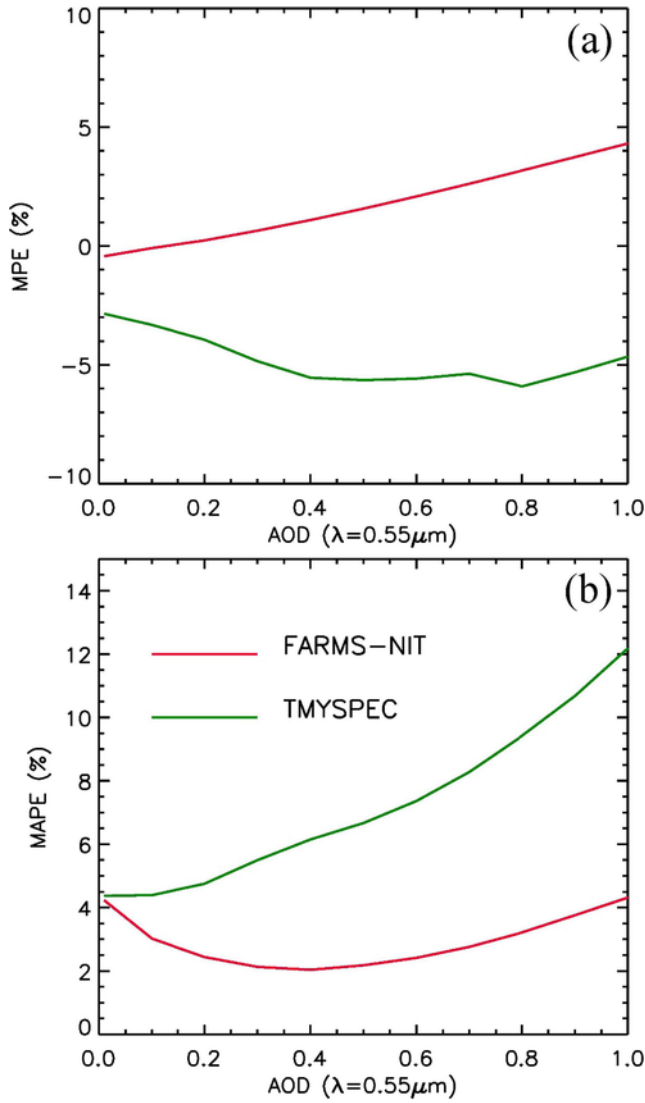
Fig. 9. (a) MPE and (b) MAPE of FARMS-NIT and TMYSPEC evaluated by the simulations by DISORT. The AOD varies from 0 to 1, and the other atmospheric properties and PV orientation are the same as in Fig. 8.
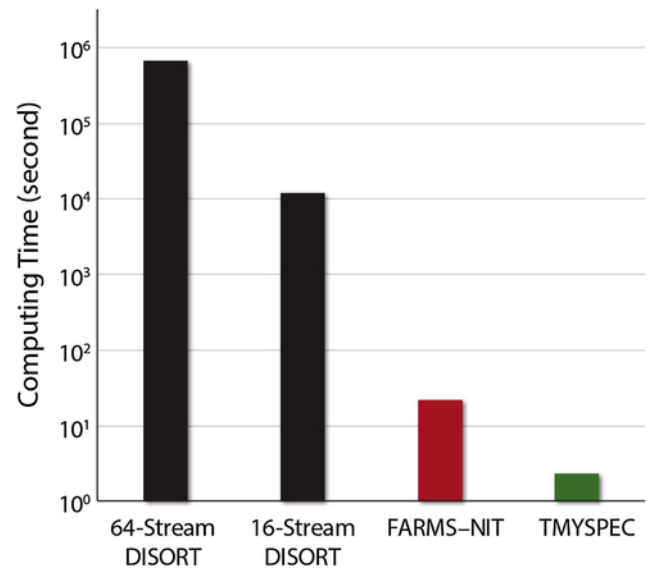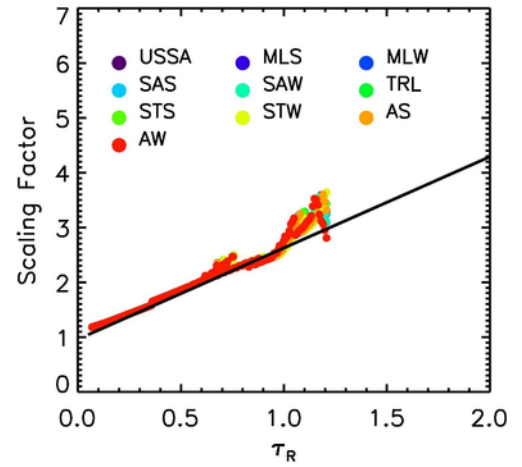
2.4. Further simplification

From the derivation above, the computation of atmospheric transmission and reflection has been substantially simplified compared to the solutions of the radiative transfer equation with the multiple scattering term (Liou, 2002). Some approximations and simplifications can be made to further reduce the computing burden of the model.

In the previous equations, we use $\mu = 1.0, 0.96, 0.92,\ldots,0.0$, and $\varphi = 0°, 10°, 20°,\ldots,360°$ for the numerical computation of the integrals. They are determined to best balance the computational efficiency and the accuracy in representing the integrals. The uncertainty associated with this selection will be further discussed in Part II (the companion paper).

Because of the double integration loop in Eq. (5b), the computation of TF_{1b} consumes most of the computational efforts of the FARMS-NIT. To simplify Eq. (5b), we assume that the solar radiation through the Rayleigh scattering in Fig. 3b is isotropic and that the downwelling irradiance is the same with the rigorous solution of the Rayleigh scattering. Then TF_{1b} can be approximated by

$$TF_{0t}^{a}{}' = \frac{\omega_a}{4} P_{0t}^{a} \frac{1}{(\mu_0 - \mu_t)} \left[\exp\left(-\frac{\tau_a}{\mu_0}\right) - \exp\left(-\frac{\tau_a}{\mu_t}\right) \right] \frac{T_{0u}^{a}}{T^{a}} \tag{16a}$$

$$TF_{jt}^{a}{}' = \frac{\omega_a}{4} P_{jt}^{a} \frac{1}{(\mu_j - \mu_t)} \left[\exp\left(-\frac{\tau_a}{\mu_j}\right) - \exp\left(-\frac{\tau_a}{\mu_t}\right) \right] \frac{T_{0u}^{a}}{T^{a}}, \tag{16b}$$

where T^a is the diffuse transmittance of aerosol computed by integrating the BTDF from Eq. (9a):

$$T^a = \int_0^{2\pi} \int_0^1 TF_{0t}^{a} \mu_t d\mu_t d\varphi_t. \tag{17}$$

$$\mathrm{TF}_{1b} = TF_{0u}T_{uu}^a, \tag{18}$$

where T_{uu}^a is the transmittance of aerosol for diffuse radiation. TF_{0u} is the diffuse transmittance of the clean atmosphere (aerosol free) where the incident is direct radiation. Thus. it can be given by the expression of TF_{1b} when $TF_{jt}^a = 1$ for all directions:

$$TF_{0u} = \frac{\omega_1}{4\pi} \int_0^{2\pi} \int_0^1 \frac{\mu_j}{\mu_j - \mu_0} P_{0j} \left[exp\left(-\frac{\tau_1}{\mu_j}\right) - exp\left(-\frac{\tau_1}{\mu_0}\right) \right] d\mu_j d\varphi_j. \tag{19}$$

To reduce the computational time, TF_{0u}/ω_1 is precomputed for all possible μ_0 and τ_1 using Eq. (19). For given atmospheric information, TF_{0u} can then be rapidly checked from the results using τ_1 and ω_1 provided by SMARTS. Fig. 4 illustrates the computed TF_{0u}/ω_1 as a function of μ_0 and τ_1. It shows that, when the atmosphere is optically thin, the diffuse transmittance increases with solar zenith angle because of the more significant Rayleigh scattering. When the optical thickness of the atmosphere is much greater than 1, the diffuse transmittance is almost negligible because of the stronger absorption in the atmosphere. T_{uu}^a used by Eq. (18) can be computed by

$$T_{uu}^a = \frac{2\pi \int_0^1 \mu \mathrm{IT}_{0u}^a d\mu}{\pi I} = 2 \int_0^1 \mu \mathrm{T}_{0u}^a d\mu, \tag{20}$$

where I represents diffuse radiance above the aerosol, and T_{0u}^a is given by Eq. (15).

3. Performance evaluation

3.1. Comparison to SMARTS for a clean atmosphere

Following the discussions above, SMARTS can provide the optical properties of trace gases and aerosols in the atmosphere based on a pre-developed parameterization and a given atmospheric profile. SMARTS also parameterizes the absorption by the molecular species, Rayleigh scattering, atmospheric reflection and land-surface reflection and efficiently uses them to compute spectral irradiance on the land surface. FARMS-NIT employs the optical properties of the atmosphere from SMARTS, solves the radiative transfer equation with the single-scattering approximation, and computes radiances for various orientations.

Although SMARTS and FARMS-NIT use completely different approaches to account for the light scattering in the atmosphere, their difference should be significantly reduced when the thickness of aerosol is negligible. Further, the computation of multiple-scattering by FARMS-NIT is improved by a correction using SMARTS. Thus, it is first important to evaluate FARMS-NIT using SMARTS with a clean atmosphere—i.e., cloud and aerosol are absent in the atmosphere.

Fig. 5 shows spectral irradiances of a clean atmosphere on a horizontal surface when solar zenith angles, θ_0, are 15° and 60°. The atmospheric properties follow the 1976 U.S. Standard Atmosphere. The figure shows that FARMS-NIT has an excellent agreement with SMARTS for all wavelengths even though they use different schemes to calculate Rayleigh scattering. The majority of the differences are localized in the UV regions, because of the considerable optical thickness of Rayleigh scattering. For the smaller solar zenith angle, FARMS-NIT gives slightly larger irradiances than SMARTS whereas the reverse is observed in the larger solar zenith angle. The maximum differences between FARMS-NIT and SMARTS are about $20\,\mathrm{Wm}^{-2}\mathrm{\mu m}$.

3.2. Validation against surface observations

To further understand the performance of FARMS-NIT, we compare model simulation with surface observation from the National Renewable Energy Laboratory's (NREL's) Solar Radiation Research Laboratory (SRRL). Fig. 6a and b demonstrate measured GHI by a Kipp and Zonen CM Pyranometer 22 (CMP22) and cloud fraction from a Yankee total sky imager on October 20, 2017 and January 22, 2018. Scenes corresponding to a smooth GHI curve and cloud fractions smaller than 20% (those in the gray shadow in Fig. 6) are selected for the clear-sky computation. Surface observations of precipitable water vapor (PWV) measured by a Zephyr Geodetic GPS antenna, AOD estimated by a seven-channel Prede POM-01 photometer, and land surface albedo from an inverted CMP21 are used as inputs to FARMS-NIT (Fig. 6c and d). As shown in Fig. 6d, a day with a snow land surface (with very large surface albedos) is selected to compare with a day when the land is covered by bare soil and vegetation (Fig. 6c).

As discussed in Section 2, FARMS-NIT employs SMARTS to compute the optical properties of aerosol, which provides twelve choices of aerosol models introduced by Shettle and Fenn (1979), IAMAP (1986), and Braslau and Dave (1973). The AODs in the narrow wavelength bands are computed using the given aerosol model, AOD in the wavelength of $0.55\,\mathrm{\mu m}$, and the Ångström's turbidity formula (Liou, 2002). In this study, we select the rural aerosol model given by Shettle and Fenn (1979) because of the low concentration of soot and sea salt particles in the atmosphere over NREL's SRRL. The model simulation by FARMS-NIT is then validated by surface observation from an EKO WISER spectroradiometer system on a single-axis tracker at NREL's SRRL that covers the wavelengths from 0.35 to $1.65\,\mathrm{\mu m}$, in 1 nm intervals (1301 wavelength bands).

For comparison with the FARMS-NIT simulations, we use the TMYSPEC model (Myers, 2012) to compute spectral irradiances in the wavelengths from 0.3 to $1.8\,\mathrm{\mu m}$, in 10 nm intervals (151 wavelength bands). The measured GHI and DNI computed by the DISC model (Maxwell, 1987) are used as the input data to TMYSPEC. Unlike FARMS-NIT, TMYSPEC combines multiple steps and empirically determined regressions to compute spectral POA irradiances from broadband GHI, DNI, and other atmospheric properties. It computes spectral irradiances in clear-sky conditions by best matching surface observations from a Li-Cor model Li-1800 spectrometer (Nann and Riordan, 1991). The spectral irradiances over tilted surfaces are corrected according to a broadband transposition model developed by Perez et al (1987). The spectral irradiances in cloudy-sky conditions are estimated by the clear-sky irradiances and an empirically determined cloud cover modifier (CCM). More details about TMYSPEC can be found in Myers (2012).

Fig. 7a and b illustrate the model simulations from FARMS-NIT and TMYSPEC. Compared to the 151 wavelength bands of TMYSPEC, the 2002 bands of FARMS-NIT demonstrate much more details of the atmospheric absorption by molecular species, e.g. the strong absorption by oxygen at the wavelength of $0.76\,\mathrm{\mu m}$ is more obvious from the results of FARMS-NIT. The model simulations and surface observations are averaged in each 20 nm interval within 0.3–$1.65\,\mathrm{\mu m}$ (66 intervals), and their differences are compared (Fig. 7c and d). FARMS-NIT better represents the peak of spectral radiation in the visible region, but it tends to overestimate the solar radiation in the UV region. However, TMYSPEC also underestimates spectral radiation in the UV region with the same order of magnitude. Note that the validation study of SMARTS also demonstrated significant uncertainties in the wavelengths of 0.3–$0.55\,\mathrm{\mu m}$ (Gueymard, 1995). Thus, future studies on improving trace gas measurements and the simulation of the atmospheric absorption are needed for both SMARTS and FARMS-NIT. For land surface covered by snow, FARMS-NIT has a much better performance than

TMYSPEC because it efficiently uses the observations of surface albedo and thus better simulates the diffuse radiation from the land surface (Fig. 7d). This is also obvious in the mean bias error (MBE), mean absolute error (MAE), percentage error (PE), absolute percentage error (APE), mean percentage error (MPE), and mean absolute percentage error (MAPE) of the model simulations (Table 1), which are defined as follows:

$$MBE = \frac{1}{n}\sum_{i=1}^{n}(POAI_M - POAI_S \tag{21a}$$

$$MAE = \frac{1}{n}\sum_{i=1}^{n}|POAI_M - POAI_S| \tag{21b}$$

$$PE = \frac{\sum_{i=1}^{n}(POAI_M - POAI_S)}{\sum_{i=1}^{n}POAI_S} \times 100\% \tag{21c}$$

$$APE = \frac{\sum_{i=1}^{n}|POAI_M - POAI_S|}{\sum_{i=1}^{n}POAI_S} \times 100\% \tag{21d}$$

$$MPE = \frac{1}{n}\sum_{i=1}^{n}\frac{POAI_M - POAI_S}{POAI_S} \times 100\% \tag{21e}$$

$$MAPE = \frac{1}{n}\sum_{i=1}^{n}\left|\frac{POAI_M - POAI_S}{POAI_S}\right| \times 100\%, \tag{21f}$$

where n is the total number of data points for all the wavelengths in one day, and the subscripts "M" and "S" represent model simulation and surface observation, respectively. As shown in Table 1, FARMS-NIT has significantly smaller uncertainties than TMYSPEC for all the statistical measures in Table 1.

3.3. Validation against DISORT for variable AOD

The discrete ordinates radiative transfer (DISORT) model (Stamnes et al., 1988) is based on a solution of the radiative transfer equation pioneered by Chandrasekhar (Chandrasekhar, 1950). By replacing the integral of the radiative transfer equation with Gaussian quadrature, solar radiances can be solved in all possible directions. DISORT has been extensively used to simulate satellite observations and understand solar and infrared radiation within the atmosphere (Hong et al., 2009; Xie, 2010; Xie et al., 2006, 2012). Similar to FARMS-NIT, DISORT directly computes POA irradiance from radiances and Eq. (2) without further approximation. With idealized input of atmospheric properties, the uncertainty of DISORT in computing radiance has been well understood and discussed in previous studies (Ding et al., 2009; Kotchenova et al., 2006). Thus, DISORT allows extending the validation to atmospheric conditions with large AOD that do not exist in our surface observations.

In the model validation using surface observations, aerosol loading around NREL's SRRL is extremely low because of the high altitude and clean air in Colorado (see Fig. 5c and d); however, this might not be applicable to other locations where surface observations are unavailable. To understand the performance of FARMS-NIT under different conditions, we apply the profile of the 1976 U.S. Standard Atmosphere to a 64-stream DISORT and FARMS-NIT that both compute the POA irradiances on October 20, 2017. A homogenous layer of aerosol with AOD varying from 0.01 to 1.0 is applied to the models. The irradiances are also computed by TMYSPEC using the broadband GHI from DISORT. Compared to DISORT, the visible peak of irradiance is slightly overestimated by FARMS-NIT (Fig. 8). The visible peak is underestimated by TMYSPEC for a thin aerosol layer (Fig. 8a), but it gradually

begins to overestimate the peak as the aerosol loading increases (Fig. 8d). For the near-infrared region, TMYSPEC underestimates irradiance, which is more significantly at higher AOD. However, the performance of FARMS-NIT is not significantly affected by the variation of AOD.

With the same atmospheric properties and PV orientation as Fig. 7, the MAPE of FARMS-NIT is stable at 2–4% even though its MPE increases with AOD from 0 to 4% (Fig. 9). The MPE and MAPE of TMYSPEC both increase with AOD; the latter can reach up to 12% when the AOD is 1.0.

3.4. Computational cost

For computing hourly spectral POA irradiances during a day, the 64-stream DISORT, 16-stream DISORT, FARMS-NIT, and TMYSPEC consume 650880.0 s (180 h 48 min), 11912.7 s (3 h 18 min 32.7 s), 21.9 s, and 2.31 s, respectively (Fig. 10) using a single Intel Xeon processor core from the NREL's flagship high-performance computing (HPC) system. Thus, FARMS-NIT increases the computational efficiency of the current radiative transfer models by a factor of greater than 500 as compared with the 16-stream DISORT. Although FARMS-NIT requires more computational resources than TMYSPEC, it provides spectral irradiances in 2002 wavelength bands, whereas TMYSPEC has only 151 bands.

4. Conclusions

We investigated the current transposition models and spectral models for solar energy applications and suggested that those models can be combined by an improved radiative transfer model where radiances in narrow-wavelength bands are efficiently computed. Following Wang et al. (2013), we derived BTDF of a clear-sky atmosphere by considering three possible paths of photon transmission and solving the radiative transfer equation with the single-scattering approximation. An efficient radiative transfer model, FARMS-NIT, was developed by parameterizing the transmission due to multiple-scattering in the UV and visible regions and further simplifying the numerical integrations.

The performance of FARMS-NIT is validated against surface observations at NREL's SRRL, spectral models for solar energy applications, and a physics-based radiative transfer model that is often used to simulate satellite observations. When cloud and aerosol are absent in the atmosphere, FARMS-NIT yields spectral irradiances very similar to those from the SMARTS model on a horizontal surface. For POA irradiances received by a single-axis tracking system, FARMS-NIT produces results in better agreement with surface observations than TMYSPEC, especially when the land surface at NREL's SRRL is covered by snow. For an atmosphere with enhanced aerosol loading, the uncertainty of FARMS-NIT does not significantly vary compared with a 64-stream DISORT model. However, TMYSPEC over- and underestimates spectral irradiances in visible and near-infrared regions, respectively, with its overall uncertainty increasing with AOD. For the same computation, FARMS-NIT significantly increases the computational efficiency of radiative transfer models even though it requires more computing time than TMYSPEC.

Appendix A. Derivation of TF_{1b} and TF_{1c}

For the radiative transfer equation of downward radiance with the single-scattering approximation:

$$\mu \frac{dI}{d\tau} = -I + \frac{\omega}{4\pi} F_0 P \exp\left(-\frac{\tau}{\mu_0}\right) \tag{A1a}$$

Multiple $e^{\tau/\mu}$ gives

$$\exp\left(\frac{\tau}{\mu}\right) dI = -\frac{1}{\mu} I \exp\left(\frac{\tau}{\mu}\right) d\tau + \frac{\omega}{4\pi} F_0 P \frac{1}{\mu} \exp\left(-\frac{\tau}{\mu_0} + \frac{\tau}{\mu}\right) d\tau \tag{A1b}$$

In Fig. 2b, integration from 0 to τ_1 gives

$$\int_0^{\tau_1} d\left[I\exp\left(\frac{\tau}{\mu_j}\right)\right] = \int_0^{\tau_1} \frac{\omega}{4\pi} F_0 P_{0j} \frac{1}{\mu_j} \exp\left(-\frac{\tau}{\mu_0} + \frac{\tau}{\mu_j}\right) d\tau \tag{A1c}$$

Then

$$I(\tau_1) \exp\left(\frac{\tau_1}{\mu_j}\right) - I(0) = \frac{\omega}{4\pi} F_0 P_{0j} \frac{1}{\mu_j} \int_0^{\tau_1} \exp\left(-\frac{\tau}{\mu_0} + \frac{\tau}{\mu_j}\right) d\tau \tag{A1d}$$

As $I(0) = 0$, we have

$$I_j(\tau_1) = \frac{\omega_1}{4\pi} F_0 P_{0j} \frac{\mu_0}{\mu_0 - \mu_j} \left[\exp\left(-\frac{\tau_1}{\mu_0}\right) - \exp\left(-\frac{\tau_1}{\mu_j}\right)\right] \tag{A1e}$$

The transmitted radiance through the aerosol is then

$$I_{t1b} = \frac{1}{\pi} \int_0^{2\pi} \int_0^1 I_j(\tau_1) \, TF_{jt}^a \mu_j d\mu_j d\varphi_j \tag{A1f}$$

Then

$$\begin{aligned} TF_{1b} &= \frac{\pi I_{t1b}}{\mu_0 F_0} \\ &= \frac{\omega_1}{4\pi} \int_0^{2\pi} \int_0^1 \frac{\mu_j}{\mu_j - \mu_0} P_{0j} T_{jt}^a \left[\exp\left(-\frac{\tau_1}{\mu_j}\right) - \exp\left(-\frac{\tau_1}{\mu_0}\right)\right] d\mu_j d\varphi_j \end{aligned} \tag{A1g}$$

For Fig. 2c, similar as Eq. (A1e), the transmitted radiance due to the Rayleigh scattering in the upper clear sky is

$$\begin{aligned} &I(\tau_t) \\ &= \frac{\omega_1}{4\pi} F_0 P_{0t} \frac{\mu_0}{(\mu_0 - \mu_t) \left[\exp\left(-\frac{\tau_1}{\mu_0}\right) - \exp\left(-\frac{\tau_1}{\mu_t}\right)\right]} \end{aligned} \tag{A2a}$$

The transmitted radiance through the atmosphere is then

$$I_{t1c} = I(\tau_t) \exp\left(-\frac{\tau_a}{\mu_t}\right) \tag{A2b}$$

Then

$$\begin{aligned} TF_{1c} &= \frac{\pi I_{t1c}}{\mu_0 F_0} \\ &= \frac{\omega_1}{4} P_{0t} \frac{1}{\mu_0 - \mu_t} \exp\left(-\frac{\tau_a}{\mu_t}\right) \left[\exp\left(-\frac{\tau_1}{\mu_0}\right) - \exp\left(-\frac{\tau_1}{\mu_t}\right)\right] \end{aligned} \tag{A2c}$$

Appendix B. Derivation of and

For single-scattering events within the aerosol layer, scattered radiance is similar as in Eq. (A1e),

$$I_t(\tau_a) = \frac{\omega_a}{4\pi} F_0 P_{0t}^a \frac{\mu_0}{\mu_0 - \mu_t} \left[\exp\left(-\frac{\tau_a}{\mu_0}\right) - \exp\left(-\frac{\tau_a}{\mu_t}\right)\right] \tag{B1a}$$

where 0 and t represent the incident and outgoing directions, respectively; and P_{0j}^a is the single-scattering phase function of aerosol that can be approximated by the asymmetric factor and Henyey-Greenstein phase function:

$$P_{0t}^a = \frac{1 - g^2}{\left(1 + g^2 - 2g\cos\Theta_{0t}\right)^{3/2}} \tag{B1b}$$

Then TF_{0t}^a is

$$\begin{aligned} TF_{0t}^a &= \frac{\pi I_t(\tau_a)}{\mu_0 F_0} \\ &= \frac{\omega_a}{4} P_{0t}^a \frac{1}{\mu_0 - \mu_t} \left[\exp\left(-\frac{\tau_a}{\mu_0}\right) - \exp\left(-\frac{\tau_a}{\mu_t}\right)\right] \end{aligned} \tag{B2}$$

For incident and outgoing directions, j and t, TF_{jt}^a is then

$$TF_{jt}^a = \frac{\omega_a}{4} P_{jt}^a \frac{1}{\mu_j - \mu_t} \left[\exp\left(-\frac{\tau_a}{\mu_j}\right) - \exp\left(-\frac{\tau_a}{\mu_t}\right)\right] \tag{B3a}$$

where

$$P_{jt}^a = \frac{1 - g^2}{\left(1 + g^2 - 2g\cos\Theta_{jt}\right)^{3/2}} \tag{B3b}$$

Appendix C. The multiple-scattering effect in Rayleigh scattering

The computation of TF_1 in Eqs. ((4)–(8)) assumes that Rayleigh scattering can be considered as single-scattering events in the atmosphere. However, multiple scattering can be significant in the UV and visible regions. Thus, the computation of the partitioning transmittance of the atmosphere in Fig. 2b and c need to be adjusted to account for the multiple-scattering effect. As a first-order approximation, we introduce a scaling factor for multiple scattering to adjust the value of ω_1 and keep the first-order downwelling irradiance consistent with the simulation by SMARTS.

We consider a clean atmosphere over a black land surface (albedo = 0). The scaling factor for multiple scattering can be given by

$$M = \frac{F_1^{SMARTS}}{\int_0^{2\pi}\int_0^{\frac{\pi}{2}} I_0 TF_{1c}\sin\theta\, d\theta\, d\varphi} \tag{C1}$$

where F_1^{SMARTS} is the first-order downwelling irradiance computed by SMARTS. Note that only TF_{1c} needs to the considered in Eq. (C1) because TF_{1a} and TF_{1b} are both 0 when there is no aerosol.

Fig. C shows the computed scaling factors for multiple scattering as functions of τ_R when $0.3\,\mu m < \lambda < 0.7\,\mu m$. The colors of the dots represent the ten reference atmospheric profiles used by SMARTS, including U.S. Standard Atmosphere, Mid-Latitude Summer, Mid-Latitude Winter, Sub-Arctic Summer, Sub-Arctic Winter, Tropical, Sub-Tropical Summer, Sub-Tropical Winter, Arctic Summer, and Arctic Winter. For simplicity, they are represented by USSA, MLS, MLW, SAS, SAW, TRL, STS, STW, AS, and AW in Fig. C. The figure shows that the scaling factor has a clear linear relationship with τ_R, and it does not significantly vary with the selection of the atmospheric profile. To give a simple parameterization of ω_1, we select a linear function of τ_R:

$$M = 1.6232711\tau_R + 1.0439955 \tag{C2}$$

which best fit the computation for USSA. Eq. (C2) is denoted by a black line in Fig. C1 where it results in minor uncertainties in all the simulations.

Note that strong multiple scattering exists in the wavelengths of $0.28\,\mu m < \lambda < 0.3\,\mu m$ where the computed scaling factor widely oscillates around the fitting curve in Eq. (C2); however, it is not related to substantial uncertainties because the spectral irradiances are small in this region. Also note that Rayleigh scattering is less noticeable when compared to the direct radiation in the wavelengths of $0.7\,\mu m < \lambda < 4.0\,\mu m$. Thus, the scaling factor is assumed as 1 for the region of $0.28\,\mu m < \lambda < 0.3\,\mu m$ and $0.7\,\mu m < \lambda < 4.0\,\mu m$.

References

Badescu, V., 2002. 3D isotropic approximation for solar diffuse irradiance on tilted surfaces. Renew. Energy 26, 221–223.

Braslau, N., Dave, J., 1973. Effect of aerosols on the transfer of solar energy through realistic model atmospheres. Part I: non-abosrbing aerosols. J. Appl. Meteorol. 12, 601–615.

Chandrasekhar, S., 1950. Radiative Transfer. Oxford Univ. Press, Oxford.

Clough, S., Shephard, M., Mlawer, E., Delamere, J., Iacono, M., Cady-Pereira, K., Boukabara, S., Brown, P.D., 2005. Atmospheric radiative transfer modeling: a summary of the AER codes. J. Quant. Specrtrosc. Radiat. Transfer 91 (2), 233–244.

Ding, S.G., Xie, Y., Yang, P., Weng, F.Z., Liu, Q.H., Baum, B., Hu, Y.X., 2009. Estimates of radiation over clouds and dust aerosols: optimized number of terms in phase function expansion. J. Quant. Specrtrosc. Radiat. Transfer 110 (13), 1190–1198.

Fahrenbruch, A., Bube, R., 1983. Fundamentals of Solar Cells: Photovoltaic Solar Energy Conversion. Academic Press Inc., New York.

Gueymard, C., 1987. An anisotropic solar irradiance model for tilted surfaces and its comparison with selected engineering algorithms. Sol. Energy 38, 367–386.

Gueymard, C., 1995. SMARTS2: a Simple Model of the Atmospheric Radiative Transfer of Sunshine: Algorithms and Performance Assessment. Florida Solar Energy Center Cocoa, FL.

Hong, G., Yang, P., Baum, B.A., Heymsfield, A.J., Xu, K.M., 2009. Parameterization of shortwave and longwave radiative properties of ice clouds for use in climate models. J. Climate 22 (23), 6287–6312.

IAMAP, 1986. A Preliminary Cloudless Standard Atmosphere for Radiation Computation. World Meteorological Organization, WMO/TD-No. 24.

Jakhrani, A., Othman, A., Rigit, A., Samo, S., Kamboh, S., 2012. Estimation of incident solar radiation on tilted surface by different empirical models. IJSRP 2 (12), 1–6.

Kotchenova, S., Vermote, E., Matarrese, R., Klemm, F., 2006. Validation of a vector version of the 6S radiative transfer code for atmospheric correction of satellite data. Part I: path radiance. Appl. Opt. 45 (26), 6762–6774.

Liou, K.N., 2002. An Introduction to Atmospheric Radiation, second ed. Academic Press, Amsterdam Boston.

Liu, B., Jordan, R., 1961. Daily insolation on surfaces tilted towards the equator. ASHRAE J. 3, 53–59.

Loutzenhiser, P., Manz, H., Felsmann, C., Strachan, P., Frank, T., Maxwell, G., 2007. Empirical validation of models to compute solar irradiance on inclined surfaces for buiding energy simulation. Sol. Energy 81, 254–267.

Maxwell, E., 1987. A Quasi-Physical Model for Converting Hourly Global Horizontal to Direct Normal Insolation. Solar Energy Research Inst, Golden CO.

McCluney, R., Gueymar, C., 1993. Sunspec 1.0 operating manual, in: Center, F.S.E. (Ed.), Cocoa, FL.

Meador, W.E., Weaver, W.R., 1980. Two-stream approximations to radiative transfer in planetary atmospheres: a unified description of existing methods and a new improvement. J. Atmos. Sci. 37, 630–643.

Mojiri, A., Taylor, R., Thomsen, E., Rosengarten, G., 2013. Spectral beam splitting for efficient conversion of solar energy—A review. Renew. Sustain. Energy Rev. 28, 645–663.

Myers, D., 2012. Direct beam and hemispherical terrestrial solar spectral distributions derived from broadband hourly solar radiation data. Sol. Energy 86 (9), 2771–2782.

Nann, S., Riordan, C., 1991. Solar spectral irradiance under clear and cloudy skies: measurements and a semiempirical model. J. Appl. Meteor. 30 (4), 447–462.

Noorian, A., Moradi, I., Kamali, G., 2008. Evaluation of 12 models to estimate hourly diffuse irradiation on inclined surfaces. Renew. Energy 33, 1406–1412.

Perez, R., Ineichen, P., Seals, R., Michalsky, J., 1990. Modeling daylight availability and irradiance components from direct and global irradiance. Sol. Energy 44, 271–289.

Perez, R., Seals, R., Ineichen, P., Stewart, R., Menicucci, D., 1987. A new simplified version of the Perez diffuse irradiance model for tilted surfaces. Sol. Energy 39 (3), 221–231.

Reindl, D., Beckman, W., Duffie, J., 1990. Evaluation of hourly tilted surface radiation models. Sol. Energy 45 (1), 9–17.

Sengupta, M., Habte, A., Gotseff, P., Weekley, A., Lopez, A., Molling, C., Heidinger, A., 2014. A physics-based GOES product for use in NREL's National Solar Radiation Database. European Photovoltaic Solar Energy Conference and Exhibition Amsterdam, Netherlands.

Sengupta, M., Xie, Y., Lopez, A., Habte, A., Maclaurin, G., Shelby, J., 2018. The National Solar Radiation Data Base (NSRDB). Renew. Sustain. Energy Rev. 89, 51–60.

Shettle, E., Fenn, R., 1979. Models for the Aerosols of the Lower Atmosphere and the Effects of Humidity Variations on their Optical Properties. Air Force Geophysics Lab, Hanscom, MA.

Stamnes, K., Tsay, S.C., Wiscombe, W., Jayaweera, K., 1988. Numerically stable algorithm for discrete-ordinate-method radiative transfer in multiple scattering and emitting layered media. Appl. Opt. 27 (12), 2502–2509.

Stokes, G.M., Schwartz, S.E., 1994. The Atmospheric Radiation Measurement (ARM) Program: programmatic background and design of the cloud and radiation test bed. Bull. Amer. Meteor. Soc. 75 (7), 1201–1221.

Wang, C., Yang, P., Nasiri, S., Platnick, S., Baum, B., Heidinger, A., Liu, X., 2013. A fast radiative transfer model for visible through shortwave infrared spectral reflectances in clear and cloudy atmospheres. J. Quant. Specrtrosc. Radiat. Transfer 116, 122–131.

Xie, Y., 2010. Study of ice cloud properties from synergetic use of satellite observations and modeling capabilities. Department of Atmospheric Sciences. Texas A&M University, College Station, TX, 150.

Xie, Y., Liu, Y.G., 2013. A new approach for simultaneously retrieving cloud albedo and cloud fraction from surface-based shortwave radiation measurements. Environ. Res. Lett. 8, https://doi.org/10.1088/1748-9326/1088/1084/044023.

Xie, Y., Liu, Y.G., Long, C.N., Min, Q.L., 2014. Retrievals of cloud fraction and cloud albedo from surface-based shortwave radiation measurements: a comparison of 16 year measurements. J. Geophys. Res. Atmos. 119 (14), 8925–8940.

Xie, Y., Sengupta, M., Dooraghi, M., 2018. Assessment of uncertainty in the numerical simulation of solar irradiance over inclined PV panels: new algorithms using measurements and modeling tools. Sol. Energy 165, 55–64.

Xie, Y., Sengupta, M., Dudhia, J., 2016. A Fast All-sky Radiation Model for Solar applications (FARMS): algorithm and performance evaluation. Sol. Energy 135, 435–445.

Xie, Y., Yang, P., Gao, B.C., Kattawar, G.W., Mishchenko, M.I., 2006. Effect of ice crystal shape and effective size on snow bidirectional reflectance. J. Quant. Specrtrosc. Radiat. Transfer 100 (1–3), 457–469.

Xie, Y., Yang, P., Kattawar, G.W., Baum, B., Hu, Y.X., 2011. Simulation of the optical properties of ice particle aggregates for application to remote sensing of cirrus clouds. Appl. Opt. 50, 1065–1081.

Xie, Y., Yang, P., Kattawar, G.W., Minnis, P., Hu, Y.X., 2009. Effect of the inhomogeneity of ice crystals on retrieving ice cloud optical thickness and effective particle size. J. Geophys. Res. 114, D11203, 11210.11029/12008JD011216.

Xie, Y., Yang, P., Kattawar, G.W., Minnis, P., Hu, Y.X., Wu, D., 2012. Determination of ice cloud models using MODIS and MISR data. Int. Remote Sens. 33, 4219–4253.